# Modelling critical Casimir force induced self-assembly experiments on patchy colloidal dumbbells

Newton, A.C.; Nguyen, T.A.; Veen, S.J.; Kraft, D.J.; Schall, P.; Bolhuis, P.G.

[Link to publication](Link to publication)

## PAPER

Check for updates

# Modelling critical Casimir force induced self-assembly experiments on patchy colloidal dumbbells†

Arthur C. Newton,[a] T. Anh Nguyen,[b] Sandra J. Veen,[b] Daniela J. Kraft, [c]
Peter Schall[b] and Peter G. Bolhuis [*a]

Colloidal particles suspended in a binary liquid mixture can interact *via* solvent mediated interactions, known as critical Casimir forces. For anisotropic colloids this interaction becomes directional, which leads to rich phase behavior. While experimental imaging and particle tracking techniques allow determination of isotropic effective potentials *via* Boltzmann inversion, the modeling of effective interaction in anisotropic systems is non-trivial precisely because of this directionality. Here we extract effective interaction potentials for non-spherical dumbbell particles from observed radial and angular distributions, by employing reference interaction site model (RISM) theory and direct Monte Carlo simulations. For colloidal dumbbell particles dispersed in a binary liquid mixture and interacting *via* induced critical Casimir forces, we determine the effective site–site potentials for a range of experimental temperatures. Using these potentials to simulate the system for strong Casimir forces, we reproduce the experimentally observed collapse, and provide a qualitative explanation for this behavior.

[a] *Van't Hoff Institute for Molecular Sciences, Universiteit van Amsterdam, Science Park 904, 1098 XH Amsterdam, The Netherlands. E-mail: p.g.bolhuis@uva.nl*
[b] *Institute of Physics, Universiteit van Amsterdam, Science Park 904, 1098 XH Amsterdam, The Netherlands*
[c] *Soft Matter Physics, Huygens-Kamerlingh Onnes Laboratory, Leiden University, PO Box 9504, 2300 RA Leiden, The Netherlands*
† Electronic supplementary information (ESI) available: Experimental particle synthesis procedure. See DOI: 10.1039/c7sm00668c

## 1 Introduction

Colloidal particles suspended in a binary liquid mixture of water and picoline (3-methylpyridine) experience an effective attraction when the temperature is raised from below towards the coexistence line of the binary mixture. As this universal attraction between colloids occurs close to the critical point of the binary liquid, it is commonly referred to as the critical Casimir force.[1,2] While the precise description of this force between suspended colloidal particles is still under debate,[3–6] this solvent mediated interaction is highly dependent on temperature, with the range of the attraction increasing as the temperature approaches the critical point.[2,7] In contrast to more common colloidal interactions such as electrostatic or depletion interactions, this temperature dependence gives precise control over the interactions between colloids. Previous work employing critical Casimir forces showed that spherical colloids can spontaneously phase separate into different colloidal phases over a small range of temperature.[7–9]

Recent breakthroughs have made it possible to synthesize anisotropic colloids[10–13] and study their behavior in binary liquids. These particles have an anisotropic shape, and/or interact *via* directional potentials. Particles of the latter category, known as "patchy particles", are able to form colloidal molecules,[12] and open crystal structures.[11] Suspensions of anisotropic colloidal particles have, therefore, great potential for the assembly of novel nano and micron-scale structures. In a recent paper we showed that the critical Casimir force can induce directional interactions between anisotropic dumbbell colloids.[14] Controlling the temperature leads to different structural morphologies, including small clusters, strings, and aggregates. At temperatures very close to the binary liquid coexistence line, a sudden collapse transition was observed.[14] *A priori*, it is not clear at all how these directional interactions can be modeled. The aim of this work is to provide an effective pair potential that is able to describe the behavior of the dumbbell system as well as to provide physical insight.

Modeling colloidal systems *via* effective pair potentials has a long history. A famous example is the DLVO theory that describes the effective interaction in colloidal suspensions as a combination of electrostatic repulsion and van der Waals attraction.[15,16] More recent examples include the depletion potential, induced by non-adsorbing polymer or other depletants, and the critical Casimir force itself.[7,17] These potentials are fundamentally isotropic in nature, allowing a description of the interaction as a potential acting on the centers of mass of the two particles. This symmetry allows extracting the effective pair potential by Boltzmann inversion

of the radial distribution function obtained from experiments *via* advanced optical imaging and particle tracking techniques. The situation is more complex for anisotropically interacting particles where such symmetry does not exist. One choice is to make the potential angular dependent, which is for example done in models such as the Kern–Frenkel model.[18] Another option, which we follow here, is to view the anisotropic particle as a rigid construction consisting of several particles that each interact *via* an isotropic potential. This is essentially a molecular viewpoint, where the constituents of the molecule are isotropic spheres, glued together to form a rigid anisotropic colloidal building block. We show that this viewpoint is suitable for the dumbbell system under consideration. We develop a simple model for the dumbbell interactions based on an isotropic form of the effective critical Casimir potential, which we then optimize, employing both reference interaction site model (RISM) theory[19–21] and direct Monte Carlo simulations, in order to reproduce variants of experimental radial distribution functions. These potentials are validated by comparing to angular distributions and *via* the predicted phase behavior. The obtained potential reproduces the different morphologies observed far from the critical temperature remarkably well. In addition, the potential gives an explanation for the structural collapse observed in the experiments when the temperature approaches the coexistence line of the binary fluid.

The remainder of the paper is as follows. In Section 2 we introduce the experimental setup, the model, and the theoretical and simulation methods. In Section 3 we present and discuss the results. We end with concluding remarks.

# 2 Methods

## 2.1 Experiments

The colloidal patchy dumbbell particles, composed of sterically stabilized PMMA spheres with a core fluorescently labelled with NBD-MAEM and a non-fluorescent shell, were prepared following the procedure laid out in ref. 14 and the ESI.† The particles were suspended in a binary liquid mixture of heavy water and picoline (3-methylpyridine, 3MP), with a weight fraction $c_{3MP} = 0.25$, below the critical composition, $c_c = 0.28$.[22] At this composition, the hydrophobic spherical ends prefer 3MP, while the hydrophilic shells prefer the water component. Glass capillaries were filled with suspensions at colloid volume fraction of 0.2%, and flame sealed to prevent any composition change due to evaporation. Critical Casimir interactions were induced by heating the suspensions to temperatures $\Delta T = T_{CX} - T$ below the coexistence temperature $T_{CX} = 38.55\ ^\circ C$ where the two solvent components 3MP and water still form a homogeneous mixture. To minimize equilibration times, we first kept the suspension at $\Delta T = 5\ ^\circ C$, where critical Casimir interactions are negligible and the particles do not aggregate. As the suspension is not density matched, particles sediment to the bottom of the capillary resulting in a quasi-2D system.

We follow particle aggregation directly in real space by imaging individual particles in an area of 104 μm × 104 μm

using confocal microscopy. For each measurement, a series of at least 3000 images was recorded for sufficient statistics. To ensure the same initial conditions (no clusters formed inside the capillary) for all measurements, we always equilibrated the system at $\Delta T = 5\ ^\circ C$ for at least 15 minutes before raising the temperature to the final desired value close to $T_{CX}$. The images were analyzed using IDL (Interactive Data Language) and the positions of the centers of the fluorescently labelled spherical ends are determined with an accuracy of 0.03 μm in the horizontal, and 0.05 μm in the vertical direction. These data sets underwent an identical analysis as the data obtained from simulations, for consistency. Distinction of dumbbells in the experiments is based on distances between spheres, which are typically 0.2–0.3 μm smaller than between neighbouring spheres, within locating accuracy and particle polydispersity. The colloidal surface charge and Debye length for the prepared suspension were determined using electrophoresis and conductivity experiments. For more details we refer to ref. 14.

## 2.2 Dumbbell model and interaction potentials

Previous work has demonstrated that the aggregation behaviour of spherical colloids in near critical binary liquids can be modelled *via* a superposition of the Casimir attraction and an electrostatic repulsion.[7,8] We extend this model towards dumbbells by modelling the particles as two touching fused hard spheres with radius $R = 1.15$ μm. The distance between the centers of mass of the spheres is thus equal to $2R$. Every pair of spheres not on the same dumbbell interacts *via* a simple potential:

$$U(r) = u_{rep}(r) + u_{att}(r), \tag{1}$$

where $r = r_{i\alpha} - r_{j\gamma}$ is the center–center distance between two spheres not belonging to the same dumbbell: sphere $\alpha = 1, 2$ of dumbbell $i$ and sphere $\gamma = 1, 2$ of dumbbell $j$. We assume that the repulsion between particles is dominated by electrostatic repulsion and a hard-sphere mechanical repulsion, so that $u_{rep}(r) = u_{HS}(r) + u_{el}(r)$, with the hard sphere $u_{HS}(r)$ potential defined as

$$u_{HS} = \begin{cases} 0 & \text{if } r > 2R \\ \infty & \text{if } r \leq 2R, \end{cases} \tag{2}$$

and the electrostatic repulsion as:[7,23]

$$u_{el}(r) = \frac{2\pi R \sigma^2 l_D^2}{\varepsilon\varepsilon_0} e^{-(r-2R)/l_D}, \tag{3}$$

where $\sigma$ is the surface charge density, $l_D$ is the Debye length, $\varepsilon$ is the dielectric constant of the solvent ($\varepsilon = 69$), and $\varepsilon_0$ is the electric permittivity in vacuum. The surface charge density, $\sigma$, and Debye length, $l_D$, have been measured *via* electrophoretic experiments which yielded $\sigma = -0.188$ μC cm$^{-2}$, and $l_D = 24.3$ nm. As the diameter of the particle is roughly 2.3 μm, these numbers correspond to a high repulsion (prefactor $\frac{2\pi R \sigma^2 l_D^2}{\varepsilon\varepsilon_0} = 6.9 \times 10^3 k_B T$) that decays relatively quickly ($l_D = 0.0211R$).

The attraction between two spherical particles is given by the Casimir interaction, which at short distances is argued by

Fisher and de Gennes to be of the form (using the Derjaguin approximation):[1,7]

$$u_{att}(r) = u_{Cas}(r) = -\frac{2\pi R k_B T}{\xi} e^{-(r-2R)/\xi}, \quad (4)$$

where $\xi$ is the correlation length of the fluctuations in composition of the near critical binary liquid. Note that the pre-factor is of the form $\xi^{-1}$. A consequence of this is that the pre-factor diverges for small correlation lengths, which is slightly counter-intuitive as the general observation is that particles become more strongly aggregated close to the critical point (large $\xi$) suggesting a stronger attraction between particles. However, due to the strong electrostatic repulsion described above only the long range effects of the Casimir attraction are important, which cancels the diverging part of the Casimir potential.

The correlation length close to the critical point of the binary liquid, $[\rho_C, T_C]$ scales with the temperature as follows:[7]

$$\xi(\Delta T) = \xi_0 \left(\frac{\Delta T}{T_C}\right)^{-\nu}, \quad (5)$$

where $\xi_0$ is the correlation length of the non-critical system, $T_C$ is the critical temperature, $\Delta T = T_C - T$ is the distance between the experimental temperature and the critical temperature, and $\nu = 0.63$ is the relevant critical exponent. Clearly, the correlation length diverges as the critical point is approached. Even when the binary liquid is prepared slightly off-critical, this scaling of the correlation length usually does approximate the behaviour well. For our system the critical temperature is set to the coexistence temperature $T_C = 38.55\ ^\circ C$. Therefore, the potential is completely defined by the parameters $R$, $\sigma$, $l_D$, $\Delta T$ and $\xi_0$. The value of $\xi_0$ is not known from experiments, and we therefore fit this value in order to describe how the potential develops when approaching the coexistence temperature.

Due to the size of the particles and because the system is not density matched, the particles easily sediment to the bottom of the sample. To mimic this situation we added a gravitational potential in the simulations

$$u_{grav}(r) = \frac{r_z}{l_{grav}} k_B T, \quad (6)$$

with $r_z$ the vertical height of the dumbbell center of mass with respect to the bottom of the box and $l_{grav} = k_B T / \Delta \rho V_{db} g$ with $\Delta \rho = 0.19\ g\ cm^{-3}$ for PMMA in water/3MP mixture, $V_{db} = \frac{8}{3}\pi R^3$ and $g = 9.81\ m\ s^{-2}$. Based on the buoyancy of the particles, we estimated the gravitational length $l_{grav} \approx 0.15R$. Periodic boundaries were only applied in the $x$ and $y$ directions, so that particles cannot sediment below $z = 0$. In addition, in the experiments the glass surface can also induce attraction, including critical Casimir forces[2] and can thus restrain particles to the surface. In this way, the system becomes effectively quasi two dimensional, as is observed in the experiments. To model this effect we added a square well potential acting on each sphere of the dumbbell

$$u_{surf}(r) = \begin{cases} 0 & \text{if } r_z > \Delta \\ -\varepsilon_{surf} & \text{if } r_z \leq \Delta, \end{cases} \quad (7)$$

with $r_z$ the vertical height of the sphere center of mass with respect to the bottom of the box, the range $\Delta = 1.7R$, and depth $\varepsilon_{surf} = 10 k_B T$. This choice of parameters roughly reproduced the observed average number of dumbbells sticking out of the plane. Moreover, if a weaker wall interaction is used spurious peaks arise in the $\theta-\phi$-distributions explained in eqn (12) below, which are not present in the experimental distributions.

For the Monte Carlo simulations the total potential energy of the dumbbell system is thus given by

$$U_{tot} = \sum_{j=1}^{N} \sum_{i<j}^{N} \sum_{\alpha,\gamma=1}^{2} u_{rep}(r_{i\alpha,j\gamma}) + u_{att}(r_{i\alpha,j\gamma})$$
$$+ \sum_{i=1}^{N} u_{grav}(r_i) + \sum_{i=1}^{N} \sum_{\alpha=1}^{2} u_{surf}(r_{i\alpha}), \quad (8)$$

where $r_{i\alpha,j\gamma} = r_{i\alpha} - r_{j\gamma}$ is the center–center distance between two spheres not belonging to the same dumbbell, and $r_i$ is the center of mass of dumbbell $i$.

## 2.3 Potential optimization

Although the parameters of the potential are connected to physical properties of the system as indicated in eqn (3) and (4), the system is not solely determined by these properties. Additional effects such as van der Waals forces and polymer repulsion could also play a role in the interaction of colloids, especially since these dumbbell particles are not synthesized to minimize these effects. Previously[8,9] the potential for spherical particles was obtained *via* fitting the potential of mean force obtained *via* inversion of the radial distribution function $g(r)$. At low density this inversion is simply $u(r) = -k_B T \ln g(r)$, where $k_B$ is Boltzmann's constant. However, several problems arise for anisotropic particles. While the one-to-one mapping between radial distribution function (RDF) and the effective pair potential still holds,[21,24] the simple inversion of the radial distribution function is not valid anymore.‡ Additional complications arise due to the fact that not all particles are accounted for, because the visualization *via* the microscope is limited to a plane. Moreover, the intrinsic error of the tracking of the particles causes an error in the particle positions. Finally, the polydispersity of the spheres and the variation in the distance between spheres of the dumbbell, play a role. Clearly, we can not use a direct fitting procedure to obtain the anisotropic potential. However, it is still possible to find an optimal effective potential by predicting the radial distribution function for anisotropic particles by simulation or theory, and compare these predicted distributions to the experimental one, and determine which potential parameters gives the best match.

For this purpose we propose several distribution functions to compare between simulations and experiment. From the experimental imaging techniques we determine the 2D site–site

---

‡ This statement applies to the orientationally averaged distribution function. In principle, one could invert the orientational and radial resolved RDF. However, this requires an extremely accurate experimental (or numerical) multidimensional data set.

radial distribution $g_{\alpha\gamma}(r)$ between sphere $\alpha = 1, 2$ on dumbbell $i$ and sphere $\gamma = 1, 2$ on a different dumbbell $j$, defined as

$$g_{\alpha\gamma}(r) = \rho^{-2}\langle N(N-1)\delta(r_{i\alpha})\delta(r_{j\gamma} - r)\rangle, \tag{9}$$

where $\delta(r)$ denotes the Dirac delta function, $\rho$ is 2D particle density (the number of particles per area), and the angular brackets denote an ensemble average over all configurations. The probability to find a site $\gamma$ a distance $r$ away from site $\alpha$ (with $\alpha$ and $\gamma$ on different molecules) is thus $2\pi r \rho g_{\alpha\gamma}(r)$. This distribution can be connected with the well-known reference interaction site model (RISM) integral equation theory for molecular fluids.[21] This distribution is estimated from the experimental data by evaluating

$$g_{\alpha\gamma}(r) \approx \frac{1}{n_f}\sum_k^{n_f}\frac{1}{N_k(N_k-1)}\sum_{i<j}^{N_k}\sum_{\alpha,\gamma=1}^{2}\frac{\delta(r_{i\alpha,j\gamma}-r)}{f(r_{i\alpha},r_{j\gamma})}, \tag{10}$$

with $n_f$ the number of frames, $N_k$ the number of dumbbells in frame $k$, $f(r_{i\alpha},r_{j\gamma})$ denotes the fraction of the circle centered at ($r_{i\alpha}$ and goes through $r_{j\gamma}$) that falls inside the microscope image. This fraction corrects for the fact that particles outside the image do not contribute.

In a similar way we also measure the minimum distance radial distribution, $g_{md}(r)$, where only the minimum distance between all dumbbell pairs is counted. This distribution is estimated from the experimental data by evaluating

$$g_{md}(r) \approx \frac{1}{n_f}\sum_k^{n_f}\sum_{i<j}^{N_k}\frac{\delta(\min(r_{i1,j1},r_{i1,j2},r_{i2,j1},r_{i2,j2})-r)}{N_k(N_k-1)f(r_{i\alpha},r_{j\gamma})}, \tag{11}$$

where the min function returns the lower of its arguments. These versions of the radial distribution minimize the effect of the trivial neighbour. Note that a simple Boltzmann inversion will lead to incorrect results in both cases.

We can also use a slightly different approach and focus solely on the orientations the particles have with respect to each other when they bind, by measuring the bond-angle distributions, which should be less dependent on the standard error of determining distances given by the system. For neighboring dumbbells we define two different bond angles, $\phi_{ij} = \arccos(\mathbf{p}_i \mathbf{v}_{ij})$ and $\theta_{ij} = \arccos(\mathbf{p}_i \mathbf{p}_j)$ where the $\mathbf{v}_{ij}$ is the vector between the center of mass of the spheres (on different dumbbells) closest to each other, so that $|\mathbf{v}_{ij}| = \min(r_{i1,j1},r_{i1,j2},r_{i2,j1},r_{i2,j2})$, and $\mathbf{p}_i$ is the dumbbell vector of which the direction is given by the sphere that defines $\mathbf{v}_{ij}$ (see Fig. 1).

Through these angles many different particle orientations can be discerned and analyzed. The angular distribution is given by

$$p(\theta,\phi) = \frac{1}{n_f}\sum_k^{n_f}\sum_{i<j\in nn}^{N_k}\delta(\theta_{ij}-\theta)\delta(\phi_{ij}-\phi), \tag{12}$$

where second sum is over the bonded neighbors only.

In contrast to the radial distribution function of spherical particles in a dilute suspension, none of the three distributions eqn (10)–(12) are directly related to the effective pair potential via a simple Boltzmann inversion, i.e. taking the negative logarithm
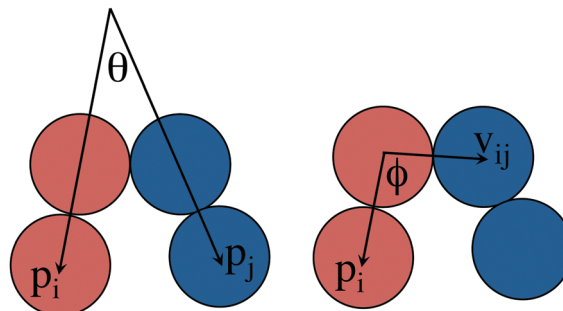


Fig. 1 Cartoon explanation of the angles $\phi$ and $\theta$ used to discern configurations between dumbbells.

of the distribution function. Therefore, we perform many Monte Carlo simulations with a predefined set of potential parameters, $\{\xi_0\}$, and subsequently find the distribution which fits best the appropriate experimental distribution. To obtain a degree of similarity between two distributions we use the Jensen–Shannon divergence:

$$d_{JS} = \sum_i P(i)\log\frac{P(i)}{M(i)} + \sum_i Q(i)\log\frac{Q(i)}{M(i)}, \tag{13}$$

where $\sum_i$ is the sum over every bin $i$, $P(i)$ and $Q(i)$ are the distributions from simulations and experiments respectively, and $M(i) = \frac{1}{2}(P(i) + Q(i))$. The potential parameters that give the smallest $D_{JS} = \sum d_{JS}(\Delta T)$, is used to construct the optimized pair-potential in eqn (1), where the sum goes over the set of temperatures used in experiment. Note that $g_{md}(r)$ and $g_s(r)$ are not normalized, so that the value for $d_{JS}$ is not bound by $\ln 2$.

### 2.4 RISM theory

We employed the reference interaction site model (RISM) theory as a first approximation to match the observed site–site radial distribution functions to an underlying potential between the dumbbell particles. While Munao et al.[25] recently investigated colloidal dumbbells in three dimensions, we followed Talbot and Tildesley,[26] who applied the RISM theory to 2D dumbbell systems. Since the experimental system is only quasi 2D we do expect some differences.

The 2D site–site correlation function is given by

$$g_{\alpha\gamma}(r) = \rho^{-2}\langle N(N-1)\delta(r_{1\alpha})\delta(r_{2\gamma}-r)\rangle, \tag{14}$$

where $\delta(r)$ denotes the Dirac delta function, $\rho$ is the 2D particle density (the number of particles per area), and the angular brackets denote an ensemble average over all configurations. The probability to find a site $\gamma$ a distance $r$ away from site $\alpha$ (with $\alpha$ and $\gamma$ on different molecules) is thus $2\pi r\rho g_{\alpha\gamma}(r)$.

Setting the total correlation function $h_{\alpha\gamma}(r) = g_{\alpha\gamma}(r) - 1$, the RISM theory defines the direct correlation function $c_{\alpha\gamma}(r)$ by a $(2 \times 2)$ Ornstein–Zernike matrix equation

$$\hat{\mathbf{h}}(k) = \hat{\omega}(k)\hat{\mathbf{c}}(k)\hat{\omega}(k) + \rho\hat{\omega}(k)\hat{\mathbf{c}}(k)\hat{\mathbf{h}}(k), \tag{15}$$

where the hats denote 2D Fourier transforms, also known as Hankel transforms,

$$\hat{f}(k) = 2\pi \int_0^\infty f(r) J_0(kr) r \mathrm{d}r \tag{16}$$

$$f(r) = \frac{1}{2\pi} \int_0^\infty \hat{f}(k) J_0(kr) k \mathrm{d}k, \tag{17}$$

with $J_0(x)$ denoting the zeroth order Bessel function. The elements of the $\boldsymbol{\omega}$ matrix are

$$\omega_{\alpha\gamma}(k) = \delta_{\alpha\gamma} + (1 - \delta_{\alpha\gamma}) J_0(kl), \tag{18}$$

with $l$ the intramolecular distance between the centers of mass of particles in one dumbbell. Because dumbbells are homo dimers all site–site correlations are identical and the RISM equation reduces to a single scalar equation:

$$\hat{h}(k) = \hat{\omega}(k)\hat{c}(k)\hat{\omega}(k) + 2\rho\hat{\omega}(k)\hat{c}(k)\hat{h}(k), \tag{19}$$

where $\hat{\omega}(k) = 1 + J_0(kl)$ and the density is now the sphere density rather than the dumbbell density. Rearrangement leads to an expression for the direct correlation function

$$\hat{c}(k) = \frac{\hat{h}(k)}{\hat{\omega}(k)^2 + 2\rho\hat{\omega}(k)\hat{h}(k)}. \tag{20}$$

Like in any integral equation approach this OZ-like equation needs a closure relation. Since we consider particles with long range interactions (relative to the hard sphere interaction), a reasonably good closure is the hypernetted chain (HNC) approximation[27]

$$g(r) = h(r) - 1 = \mathrm{e}^{-\beta u(r) + h(r) - c(r)}. \tag{21}$$

Eqn (20) and (21) form a closed set, and allow the computation of the $g(r)$ from a given $u(r)$. The solution is obtained numerically, by iteration, mixing in the previous solutions of $h(r)$ at each iteration step. The $u(r)$ is optimized using the Jensen–Shannon divergence of the computed final $g(r)$ and the experimental $g(r)$. For comparison of the computed and experimental distributions, the computed $g(r)$ is convoluted with a Gaussian function of width $w$, to mimic the experimental error. During the optimization $\xi_0$ as well as the width $w$ were varied.

### 2.5 Simulation details

For the direct Monte Carlo simulations, we placed $N = 100$ dumbbell particles in a cubic box and applied periodic boundaries in the $x$–$y$ direction. The number of particles was chosen to correspond roughly to the experimentally observed number of dumbbells. The gravitational and square well potential acted in the $z$-direction, as describe above. The size of the box was set to $L = 64R$, chosen such that the number density of the cubic box is $\rho = 0.0004R^{-3}$, and the 2D number density $\rho = 0.025R^{-2} = 0.02~\mu\text{m}^{-2}$. In order to minimize hysteresis during aggregation we employed an annealing procedure. Starting far from $T_C$, at $\Delta T = 1.6$ K where the attraction is very shallow, we performed $10^6$ equilibration and $10^6$ production cycles, where a cycle consist of moving each particle once on average, before increasing the temperature with 0.05 K. This procedure was repeated until $\Delta T = 0.85$ K, corresponding to a strong Casimir attraction. The

Monte Carlo moves were comprised of single particle translation and/or rotation moves, augmented with cluster moves.[28] A MC cycle consists of $N$ particle rotations or translations, and $N$ cluster moves. Cluster movers were performed using the algorithm in ref. 29. The maximum translation and rotation were optimized to achieve an acceptance ratio between 20% and 70%. We performed this scheme for $\xi_0 = 9.2 \times 10^{-4}~\mu\text{m}$ to $\xi_0 = 20.7 \times 10^{-4}~\mu\text{m}$ with increments $\Delta\xi_0 = 1.15 \times 10^{-5}~\mu\text{m}$.

For the diffusion limited aggregation simulations to study the collapse transition from a network structure, we first start with cluster moves only, so that the clusters do not relax internally. A particle belongs to a cluster if its center of mass is within a distance $2R + 0.23 = 2.55~\mu\text{m}$ of the center of mass of any particle in that cluster. We then relaxed the obtained DLA network structure using single particle moves and rotations with very small maximal translation and rotation displacements, until the local energy minimum was reached.

## 3 Results and discussion

### 3.1 Potential optimization

**3.1.1 RISM approach.** As an initial step we used the RISM approach to optimize the potential, using the Jensen Shannon divergence between the experimental and predicted site–site RDFs. Note that in order to properly compare experimental distributions to either theoretical predictions or simulations, the experimental error needs to be taken into account. This experimental error arises from uncertainty in measuring the positions of the center of the spheres, polydispersity in particle size and variation in the intramolecular distance between the dumbbell spheres. As the size of the particles is around 2.3 μm, the range of the attraction far from the coexistence temperature ($\Delta T \approx 1$ K) point given by the optimized potential is small relative to the size of the particle. In contrast, the broad first neighbour shell peak in the experimental $g_{\text{md}}(r)$ and $g_s(r) \equiv g_{\alpha\gamma}(r)$ would suggest a much larger attractive range. However, the observed fluctuations in bond distance of two bound dumbbells in the experimental image sequence are commensurate with the width of the optimized potential, and not with the broad first peak in the radial distribution. This suggests that the broadness of the peak is introduced by the polydispersity in particle size and shape, and the measurement error. To mimic this error we convolve the RDF with a Gaussian function with width $w$. The number density in the plane is set to $\rho = 0.025~\mu\text{m}^{-2}$.

The results of the RISM optimization are shown in Fig. 2. Fig. 2c shows the Jensen–Shannon divergence for the different $\xi_0$ and $w$ values. The global minimum is obtained around $\xi_0 = 16.3 \times 10^{-4}~\mu\text{m}$ and $w = 0.16R$ (meaning $w = 0.08$ in units of the diameter). The potentials corresponding to the optimum are shown in Fig. 2a. Note that the potentials are relatively short ranged compared to the particle size. Far from the coexistence temperature $\Delta T = 1.55$ K the attraction has a minimum of about $0.5k_BT$. As the temperature increases, the potential gradually deepens and widens. The predicted and broadened site–site $g(r)$s are shown in Fig. 2b together with the experimental
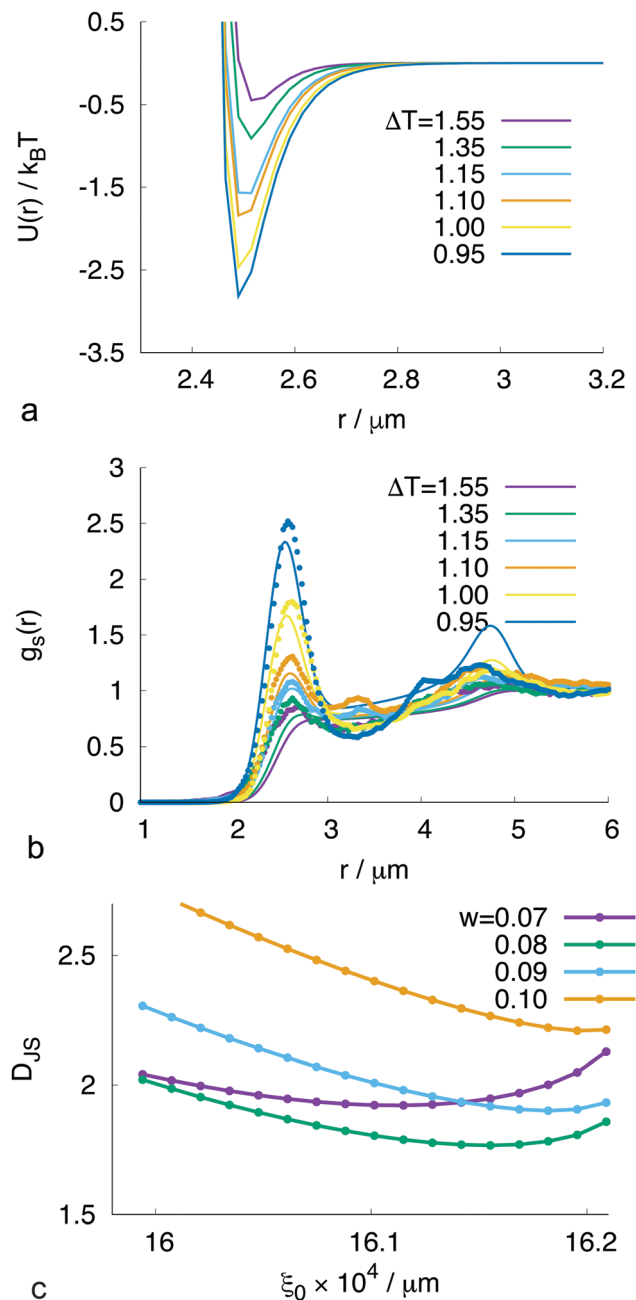
Fig. 2 (a) optimized potentials obtained from the measured site–site RDFs using RISM. (b) Comparison of predicted (lines) with experimental (points) site–site radial distribution functions. (c) Jensen–Shannon divergence for different $\xi_0$ and $w$ values. Note that the $w$ values are in units of diameter of the particle.

accurate compared to the RISM results, as they are performed in 3D, and mimic the experimental situation to a much better degree. Again the predicted radial distribution functions were convoluted with a Gaussian of width $w$ to take into account the effect of the experimental measurement errors.
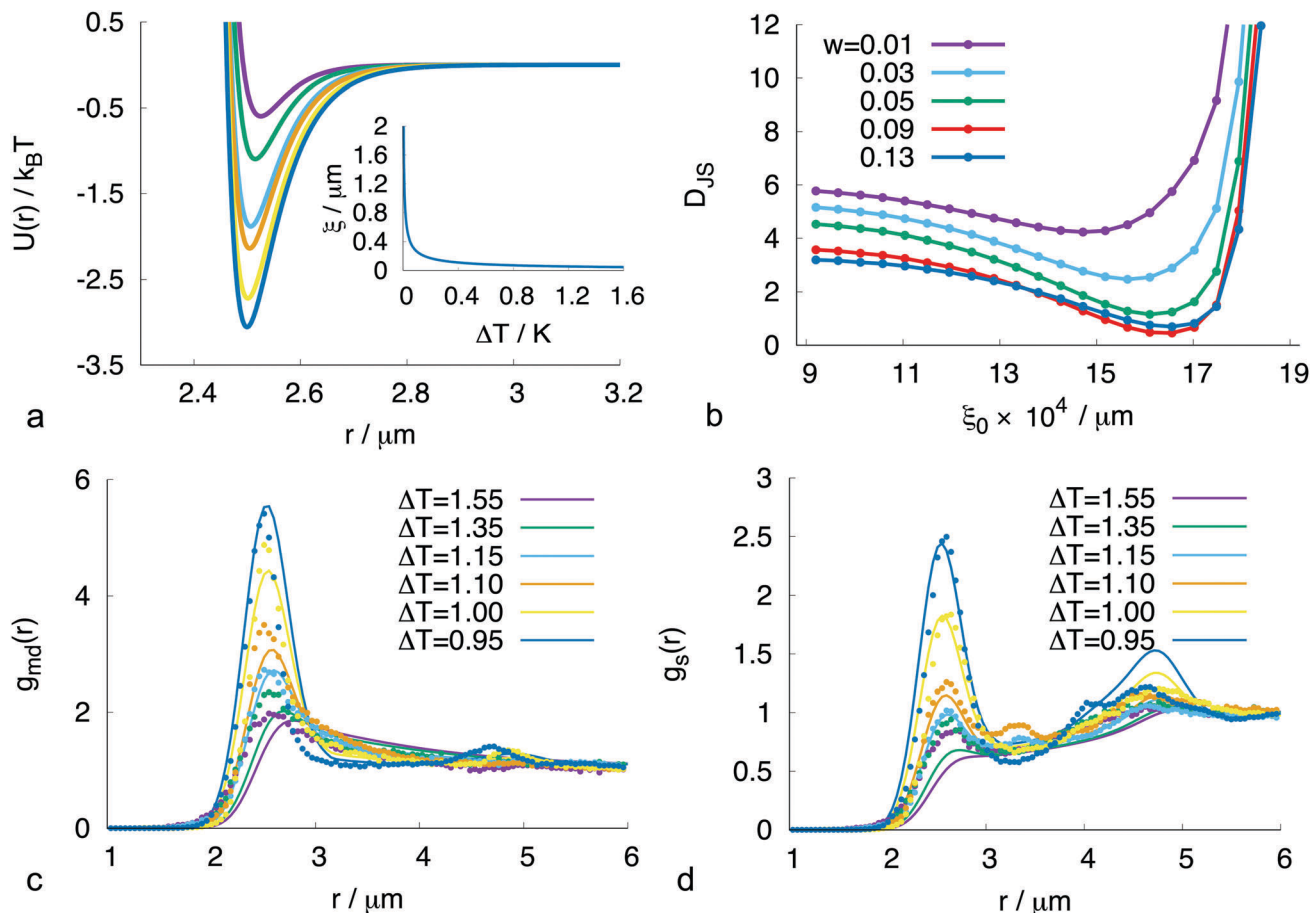
In Fig. 3 the $D_{JS}$ values found for various $\xi_0$ and $w$ are plotted when using $g_{md}(r)$ to optimize which demonstrates that $\xi_0 = 16.5 \times 10^{-4}$ µm = 1.65 nm and $w = 0.18R$ yields the best fit. This value defines the effective pair sphere–sphere potential given by eqn (1) over the entire temperature range. Fitting to the $g_s(r)$ radial distribution also yielded a fitted value of $\xi_0 = 16.5 \times 10^{-4}$ µm. The value of $\xi_0$ is on the same order as has been found in previous work.[30] The site–site effective pair potentials $u_{ij}(r)$ are plotted in Fig. 3 clearly showing the weak interaction at low temperature $\Delta T = 1.55$ K which deepens and develops a longer range when the temperature is raised closer to the coexistence temperature.

The corresponding $g_{md}(r)$ and $g_s(r)$ are presented in Fig. 3c and d. As in the case for the RISM optimization, a reasonable match is found for most temperatures. However, there are also differences with the RISM results, due to the approximations made in the theory. For instance, it seems that the optimized potential is too weak for $\Delta T = 1.55$ K and $\Delta T = 1.35$ K. while a very good match is found for higher temperatures for both $g_{md}(r)$ and $g_s(r)$, while in the RISM optimization it is the other way around. Also the second peak in $g_{md}(r)$ is well reproduced at high temperatures. Several features in $g_s(r)$, $e.g.$ near $r = 3.2$ µm and $r = 3.9$ µm, are not well reproduced, possibly because the model potential, although capable of describing the main features of the dumbbell particles, can not account for every signature in the radial distributions as the particle shape can deviate from the simple modeled one. Moreover, the experimental data set itself is of limited size. In Appendix A we provide several geometrical explanations for these features.

### 3.2 Validation of the optimized potential

To validate the optimized potential, we compare experimental and simulation snapshots as well as the simulation predictions of the angular distributions with experimental ones, and compute the location of the condensation transition with the second virial coefficient approach.

In Fig. 4 the angular distributions are shown. The features of the distributions significantly change with temperature. At low temperature, $T = 37.00$ °C, where the attraction is minimal, the majority of the population is in the top right corner at high $\theta$ and high $\phi$, which corresponds to bonds being formed in a linear orientation. As temperature increases, the degree of aggregation also increases and the population shifts from high $\theta$ and high $\phi$, to two peaks at $\theta = 0°$ and $\phi = 70°$ or $\phi = 110°$, which corresponds to a more closed packed bond formation. The corresponding optimized angular distributions obtained $via$ simulation are also presented. The simulated distributions show the same trend as the experimental ones, $i.e.$ the population shifts from a linear orientation towards more close packed configurations, with a hexagonal order similar to that of single spheres. Indeed, the two most right pictures represent high

measurements. There are some differences with the experimental RDFs, $e.g.$ in the height of the first peak, and some of the more detailed features. However, the location of the peaks and the qualitative behavior is in agreement. Note that the fit is global, and optimizes all potentials simultaneously.

**3.1.2 Simulation approach.** Next, we used direct Monte Carlo simulations to globally fit the potentials to the entire set of measured distributions for the minimum distance radial distribution function $g_{md}(r)$ as well as the site–site radial distribution function $g_s(r) = g_{\alpha\gamma}(r)$. These simulations are expected to be more

**Fig. 3** (a) Optimized potential for 6 values of $\Delta T$ when $\xi_0 = 16.5 \times 10^{-4}$ μm. As the critical point is approached, a minimum is developed. Note the short ranged nature of the potential due to the relative size of the correlation length and the size of the particles. Inset shows the divergence of the correlation length close to $T_C$. (b) Sum of $d_{JS}$ as a function of $\xi_0$ when fitting $g_{md}(r)$ demonstrating that the minimum is indeed at $\xi_0 = 16.5 \times 10^{-4}$ μm. Note that $D_{JS}$ is not bounded by the usual value of ln 2 due to the fact that the radial distributions are not normalized. The sharp increase at higher $\xi_0$ is due to the fact that complete aggregation occurs for these values. (c) Fitted $g_{md}(r)$ and (d) fitted $g_s(r)$ for $\xi_0 = 16.5 \times 10^{-4}$ μm demonstrating that for this value of $\xi_0$ simulations (lines) reproduce the main features and trend of the experimental distributions (points) very well. Note that the $w$ values are in units of diameter of the particle.

temperature angular distributions, where the peaks in the $\theta$–$\phi$-plane occur at multiples of 60°. The experimental and simulated distributions are qualitatively the same, although peaks are more pronounced for the simulation, most likely caused by incomplete equilibration of the experimental system.

Images from experiments in Fig. 5, showing the aggregation of particles at several temperatures, are qualitatively well reproduced by simulation. While no aggregation is observed for temperatures far from $T_C$, particles start to aggregate into clusters as the temperature is increased toward the binary liquid coexistence line. The experimental aggregation temperature is found to be around $\Delta T = 0.95$ K, something that is reproduced in the simulations.

Since the optimized potential is very short ranged, it is not so easy to understand this onset of aggregation. A simple but effective predictive measure for aggregation is the second virial coefficient, $B_2$:[31,32]

$$B_2 = \frac{1}{2} \int d\mathbf{r} \int d\Omega \left( 1 - e^{-\beta u_{db}(\mathbf{r},\Omega)} \right), \qquad (22)$$

where $\mathbf{r}$ is now the interparticle vector between centers of mass of two dumbbells, $d\Omega$ denotes the relative orientation of the dumbbells in 3D, and the inter-molecular potential is $u_{db}(\mathbf{r},\Omega) = \sum_{\alpha,\gamma=1}^{2} u(r_{\alpha\gamma}(\mathbf{r},\Omega))$, with $u(r_{\alpha\gamma})$ the effective site–site pair potential, and $r_{\alpha\gamma}$ the distance between the centers of mass of the dumbbell spheres $\alpha$ and $\gamma$ each on different dumbbells. Positioning one of the particles in the origin with its intramolecular vector along the $z$-axis, the integration is thus over all positions of orientations of the second dumbbell. Note that we can evaluate the integral in 3D as well as 2D, since the colloidal system can aggregate also in the bulk. Of special interest is the reduced second virial coefficient, $B_2^\star = B_2/B_2^{HDB}$ where $B_2^{HDB}$ is the second virial coefficient for hard dumbbells.[26,33,34] This reduced second virial coefficient provides a rough indication of the aggregation behavior. When $B_2^\star$ becomes negative, attraction begins to dominate the repulsive interactions. In Fig. 6 the numerically integrated $B_2^\star$ for the optimized potential is shown, for both the 2D and 3D cases. $B_2^\star$ becomes zero around $\Delta T = 1.0$ K for the 3D case, and around $\Delta T = 0.95$ K for the 2D case, which is
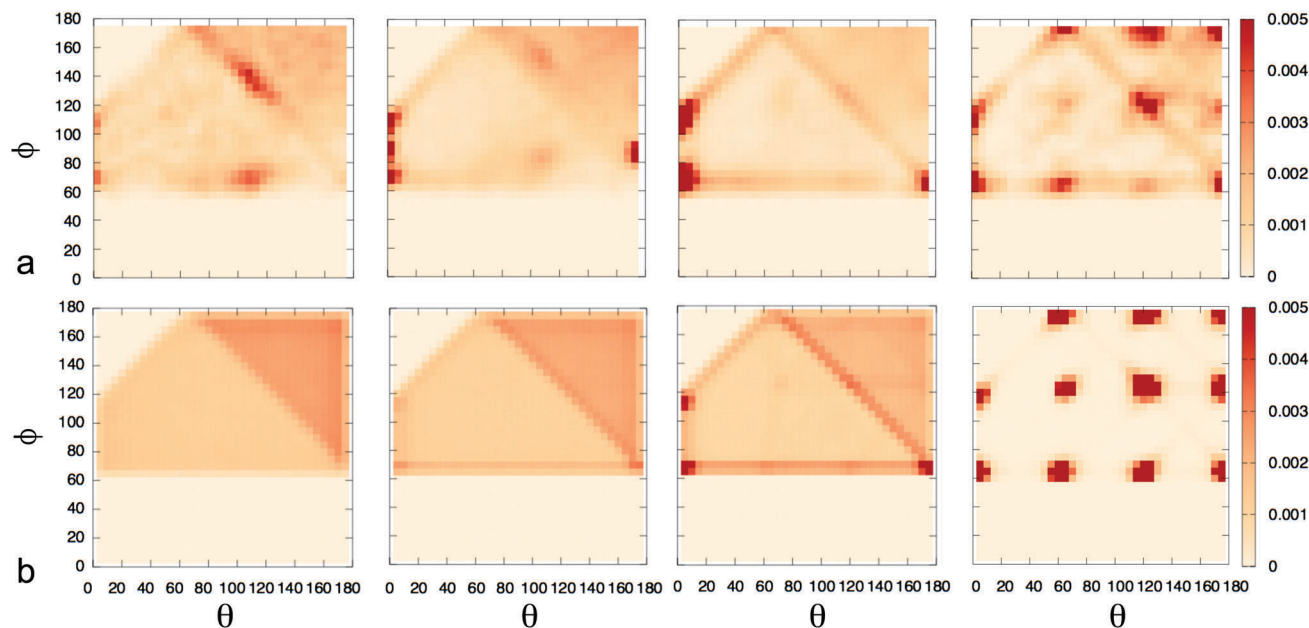
**Fig. 4** (a) Experimental and (b) simulation $\theta-\phi$ angle probability distributions for, from left to right, $\Delta T$ = 1.55 K, 1.15 K, 0.95 K, and 0.05 K. While there are differences in the angles sampled for experiments and simulation, the main features of the experimental distributions are clearly reproduced in simulations. Far from the critical point linear configurations dominate, indicated by $\theta$ = 180° and $\phi$ = 180°. As $T_C$ is approached, the population shifts to $\theta$ = 0° and $\phi$ = 70° or $\phi$ = 110°. At high temperature experiment and simulation do show peaks in the $\theta-\phi$-plane at multiples of 60°. The distributions are qualitatively the same, although the peaks are more pronounced for the simulation, most likely caused by incomplete equilibration of the experimental system.
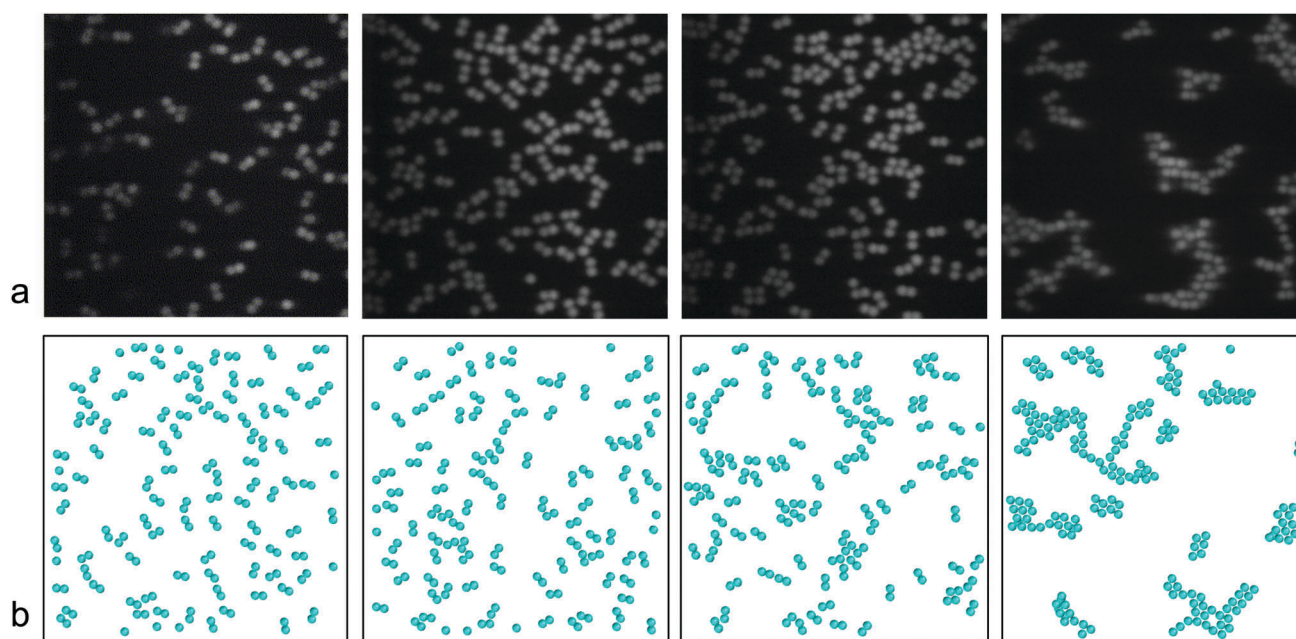


**Fig. 5** Snapshots of (a) the experiment and (b) simulation for from left to right $\Delta T$ = 1.55, 1.15, 0.95 and 0.55 K, demonstrating that the correct morphology for every temperature is (roughly) obtained.

the aggregation temperature in experiments. Further decrease of $\Delta T$ causes a fast drop of the $B_2^*$ indicating that the system is undergoing a condensation/aggregation transition in this temperature region. For completeness, we also show in Fig. 6

the reduced second virial coefficient for a system of single spheres interacting *via* the same effective potential. Clearly, the behavior is roughly similar, indicating that the geometry of the dumbbell only mildly influences the aggregation transition.
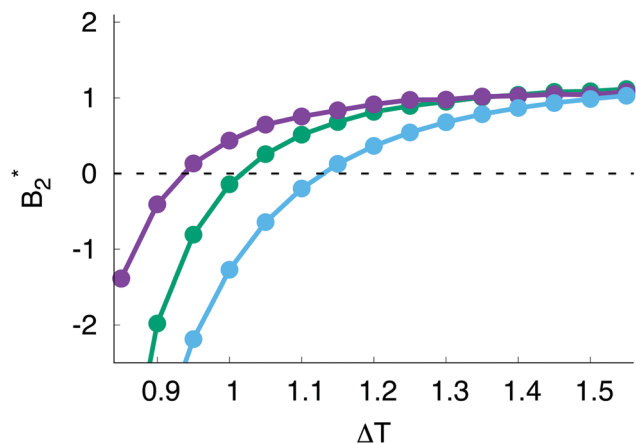
**Fig. 6** Numerical calculation of the reduced second virial coefficient $B_2^* = B_2/B_2^{HDB}$ for the optimized potential for the dumbbell model in 3D (green circles), and in 2D (purple circles). For comparison $B_2^* = B_2/B_2^{HS}$ for single spheres in 3D is also shown (blue circles). The $B_2^*$ becomes negative around $\Delta T \approx 0.95$ K for the dumbbells, which is also the aggregation temperature in experiments. Further decrease of $\Delta T$ causes a fast drop of the $B_2^*$ indicating that the experiments are close to the vapor–liquid transition in this region. Of course, for very strong attraction (lower $\Delta T$), crystallization probably occurs.

Since the potentials are short-ranged a possible colloidal liquid–vapor coexistence might be metastable with respect to crystallization. Inspecting the potentials shown in Fig. 3, a rough estimate suggests a potential range of $\sim 0.15$ μm, or around 6% of the particles diameter. A more careful mapping using the extended corresponding-states criterion by Noro and Frenkel[31] leads to an effective range of 0.04–0.05 (in units of the diameter). As the criterion for a stable liquid–vapor coexistence is around 14%,[31] it is likely that the aggregated system would relax to a colloidal vapor–solid coexistence, when equilibrated. Interestingly, when $\Delta T$ is decreased further ($\Delta T < 0.1$), the potential becomes shallower, while the range of the potential will widen. This behavior of the potential might explain the collapse as discussed in the next section.

Finally, we show in Appendix B that an optimization of the Debye length $l_D$ in the model leads to values close to the experimentally measured Debye length, giving an independent validation of the model.

### 3.3 Collapse from network to compact state

Critical Casimir forces can clearly induce aggregation between anisotropically shaped colloids. Although this aggregation is in principle reversible with temperature, the morphology of the final structure still highly depends on the protocol of the experiment. When a temperature ramp is used that takes the temperature from $\Delta T = 5.0$ K immediately to $\Delta T = 0.5$ K, thus inducing a very strong attraction, the resulting structure can become (partially) kinetically trapped in a metastable state from which it is usually very difficult to escape. In general one can anneal such a trapped state by weakening the attraction again (assuming the attraction is reversible in practice) so that the particles unbind again and the system can escape from the metastable trapped state.

While the range of the Casimir attraction, as determined by $\xi$, monotonically increases upon approaching the coexistence temperature, due to the functional form of eqn (4) the minimum of the potential does not behave monotonically with temperature, and in fact reaches a maximum depth before becoming more shallow again (see the inset of Fig. 7a). This particular feature of the potential leads to the observed experimental behavior of a structural collapse for temperatures close to the coexistence line. In Fig. 8 a sequence of snapshots is shown of such a collapse transition, from an extended network to a more compact structure. The system relaxes over several minutes, where the initial configuration on the left is stuck in a metastable state with more linear chain-like structures. For temperatures very close to $T_C$, ($\Delta T \approx 0.05$ K), the structure relaxes towards a more compact structure as shown on the right in Fig. 8.

We can model this collapse transition by preparing a non-equilibrium network-like structure using a diffusion limited aggregation scheme (see Methods), in which we only perform MC cluster moves, which are always accepted provided there is no hard core overlap. In this approach we ignore any influence of hydrodynamic effects on the kinetics. A cluster is defined as a set of contiguous particles, where we consider two dumbbells to be contiguous when any two spheres of the dumbbell are closer than $0.2R$. Starting from a random gas-like configuration, this procedure quickly results in a network structure in which the particles have not been allowed to equilibrate due to the fact that only cluster moves are used. Subsequently, this network structure is quenched into a local energy minimum dictated by the optimized pair potential at $\Delta T = 0.5$ K, employing only local single particle MC moves with small translation and rotation step sizes, such that the system becomes truly trapped in this network structure (see Fig. 8). Repeating this procedure five times generates five independent initial structures which are then further heated to the temperature of interest and subsequently relaxed via single particle translation and rotation MC moves with small step sizes ($\delta_t = 0.02R$, $\delta_r = 0.03$ rad) for $10^7$ MC cycles, where every MC cycle has $N_{part}$ translation and rotation moves. This roughly corresponds to an experimental relaxation of several minutes.[35] Snapshots of the resulting collapsed structures are shown in Fig. 8.

The analysis of these simulations is summarized in Fig. 7. The top right panel, Fig. 7b, shows the relaxation of the total energy versus simulation time for several values of $\Delta T$. It is clear that when the attraction is still short ranged, the potential does not allow equilibration of this structure to a more compact configuration, because the dumbbells only feel their local neighbourhood which is already in a deep minimum. However, as the correlation length quickly grows at very small $\Delta T$, the pair interaction also becomes more extended. Therefore, the particles have more 'wiggle' room within the potential well, allowing the Casimir force to induce a full collapse of the structure, thereby lowering the energy of the system significantly. The energy per particle normalized to the minimum ($E_{tot}(U_{min}N)^{-1}$), is plotted in Fig. 7c and clearly shows that the structure collapses only for low $\Delta T$, and thus for longer ranged attractions at small $\Delta T$, a particle thus effectively interacts with more neighbors.
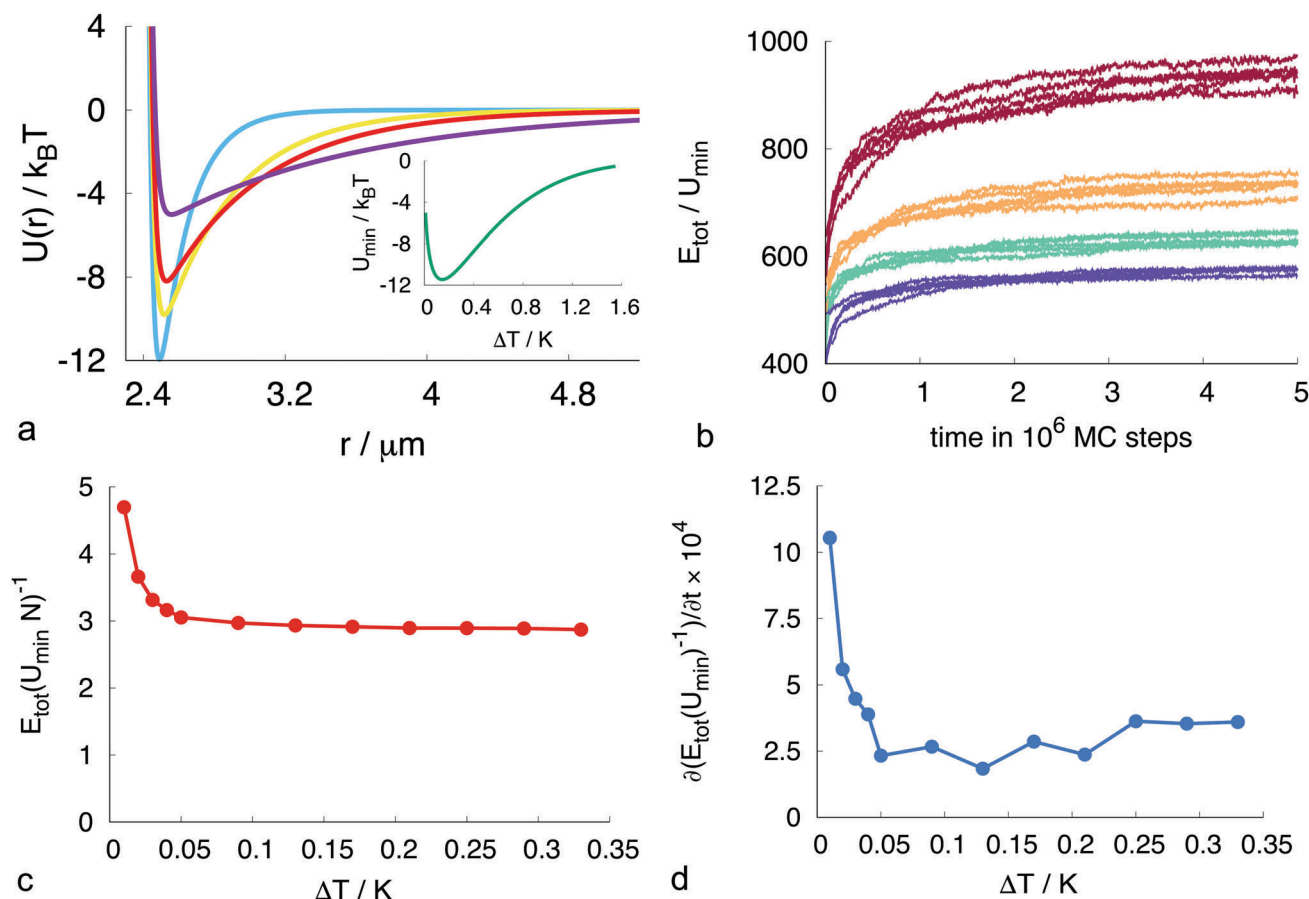
**Fig. 7** (a) Optimized potential for $\Delta T$ close to $T_C$, $\Delta T = 0.2$ K (blue), 0.05 K (yellow), 0.03 K (red), 0.01 K (purple), showing that due to the prefactor in eqn (4) the potential becomes very long ranged and flatter for small $\Delta T$, leading to the particles becoming more motile. Inset shows how the potential minimum increases close to $T_C$. (b) Relaxation of the total energy divided by minimum of attractive well over time for $\Delta T = 0.01$ K (red), 0.02 K (orange), 0.04 K (cyan) and 0.3 K (blue) starting from five different trapped network structures. (c) Sudden increase close to $T_C$ in average $E_{tot}(U_{min}N)^{-1}$ at the final time-step for each $\Delta T$ which is a measure for the number of interactions per dumbbell. (d) Slope of $E_{tot}$ divided by $U_{min}$ over time demonstrating that relaxation of energy is significantly higher close to the critical point.

The relaxation of the potential energy over time is shown in Fig. 7d, also demonstrating that indeed the energy relaxes faster for small $\Delta T$.

# 4 Conclusions

We have demonstrated that the experimentally observed Casimir induced self-assembly of colloidal dumbbells[14] can be modelled with a relatively simple potential form. We optimized this potential to reproduce both the minimum distance and site–site radial distribution function. The overall agreement between simulation and experimentally observed radial and angular distributions and structures suggests that the effective pair potential sufficiently can describe the interaction between colloidal dumbbells, at least for short-ranged potentials. For temperatures very close to the coexistence line, where the interaction becomes large (but finite), probably an effective pair potential is insufficient to describe the interaction as many body effects become important. Additionally, we have shown that the divergence of the correlation length, together with

the weakening of the potential depth is able to explain the experimentally observed collapse of locally stuck network structures into more compact configurations. These simulations allowed us to understand the experimentally observed structures from a simple pair potential model based on sphere–sphere interactions of the dumbbells. Moreover, we identify the experimental structures as partially out-of-equilibrium configurations. Future work might address the characterization of the structure and dynamics of these formed clusters, for instance by using the methods of ref. 36 and 37.

Colloidal patchy dumbbells with one patch were also considered by Avvisati *et al.*[38] Their model represented an amphiphilic dumbbell, which can self-assembly in *e.g.* micelles, bilayers, or vesicles. In contrast, our dumbbell particles have an attractive patch on either side, resulting in network-like structures and large clusters.

The universal nature of the Casimir force offers opportunities for other anisotropic colloidal systems. Future prospects entail the further modification of the particle shape and physio-chemical surface properties to induce more complex structure formation.
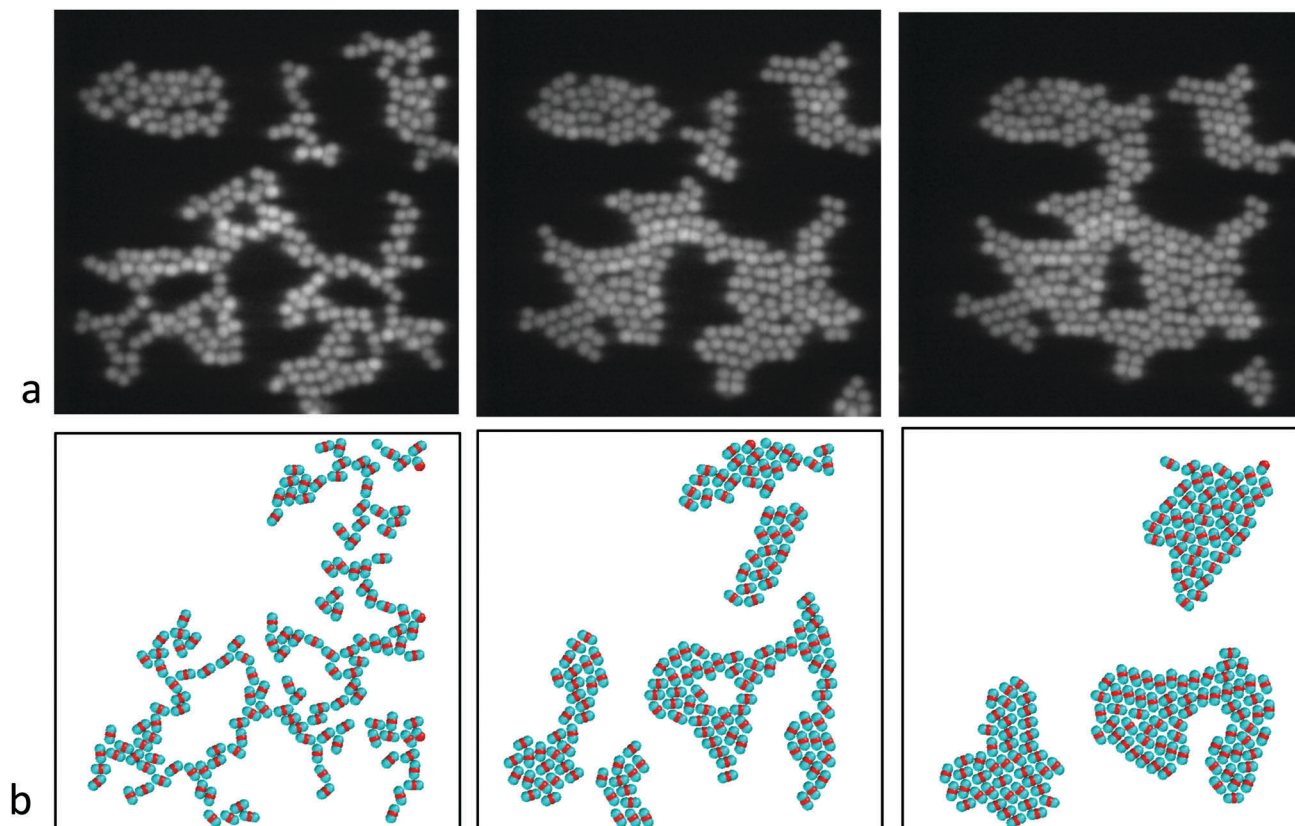
**Fig. 8** (a) Series of snapshots for a network-like structure close to the critical point. From left to right, we can see the structure relaxing towards a more compact structure facilitated by the long range nature of the Casimir force. (b) Series of snapshots for a network like structure from simulations at $\Delta T$ = 0.01 K modelling the collapse seen in experiments. Clearly, the structure fully collapses when the correlation length increases at $\Delta T$ = 0.01 K. At this point the range of the Casimir attraction is long enough such that the particles further apart begin to (partially) relax. If the correlation length remains small, such relaxation is not observed on this time-scale. Note that the system does not fully relax, as there are still multiple clusters.

Finally, we note that our potential optimization approach is independent of the origin of the interaction, and can be applied to other colloidal systems.

# Appendix

## A   Geometric interpretation of additional peaks in experimental $g(r)$

By geometric analysis and inspecting the experimental snapshots, we propose three different configurations of dumbbell pairs that can contribute to the second neighbor peaks. These
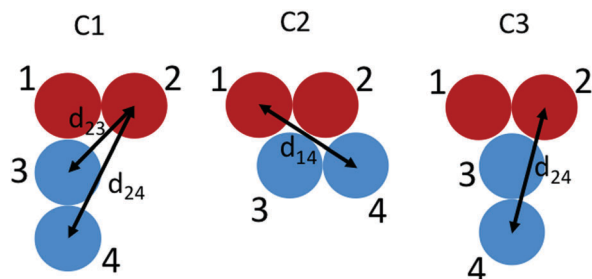


**Fig. 9** Possible configurations that contribute to the second neighbor peaks based on inspection of the experimental snapshots.

configurations, labeled C1, C2 and C3 are shown in Fig. 9. Setting the diameter of a sphere to 2.3 µm, the distance between two spheres in a dumbbell also to 2.3 µm and the minimum of the potential between two spheres is at $r_{\min}$ = 2.5 µm, means that $d_{23}$ in C1 is around 3.4 µm, which would explain the peak seen for the experimental data around this value at $\Delta T$ = 1.15 K and $\Delta T$ = 1.10 (see Fig. 3). However, in an equilibrium MC simulation, this is not a stable configuration, as it will quickly progress to either C3 or even further to C2. This demonstrates that in experiments particles in meta-stable states do not always easily find the local minimum, a fact that we also use in the DLA simulations where particles indeed are not allowed to relax. In C2, $d_{14}$ = 4 µm, which indeed also corresponds to a peak in the experimental data, and a broad shoulder in the simulation data (see Fig. 3). In C3, $d_{24}$ = 4.7 µm, which appears in both simulation and experimental $g(r)$ as a distinct peak. Due to the simple Gaussian error in the calculation of distances in the simulation, the peaks due to C2 and C3 second neighbor configurations are mixed smoothly, which does not need to be the case in reality.

## B   Dependence RISM optimization on Debye length

In the potential model we have only one free parameter that we optimize. Other important parameter such as the Debye length
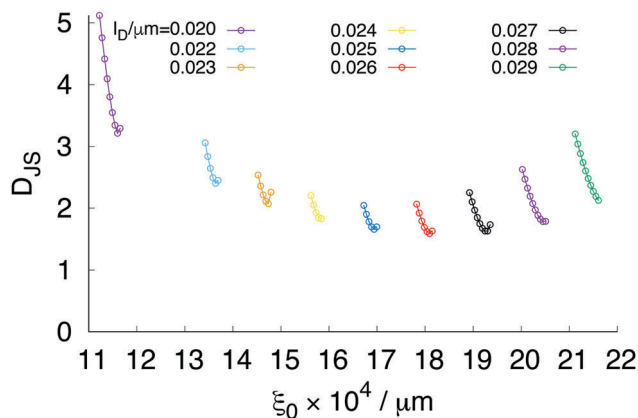
**Fig. 10** Jensen–Shannon divergence as function of $\xi_0$ for different $l_D$ values.

have been established experimentally. Still, it is interesting to investigate how sensitive the optimization is to changes in the Debye length. Therefore, we applied the RISM optimization to several values of the Debye length $l_D$ = 0.020, 0.021, 0.022, 0.023, 0.024, 0.025, 0.026, 0.027, 0.028, 0.029 μm. In this optimization we kept the Gaussian error estimate to $w$ = 0.08, which turned out optimal for all $l_D$. All other parameters were set as in Section 3.1.1. The results of the optimization is shown in Fig. 10. The optimized value $\xi_0$ changes substantially with $l_D$. This is easily understood, since a longer Debye length implies a longer ranged repulsion, and hence a longer ranged Casimir force is needed to compensate. Strikingly however, the optimal $D_{JS}$ value is obtained for $l_D$, which is actually not far away from the experimental value $l_D$ = 0.0243 μm, giving an independent validation of the model.

## Acknowledgements

## References

1  M. E. Fisher and P. G. de Gennes, *C. R. Seances Acad. Sci., Ser. B*, 1978, **287**, 207–209.
2  C. Hertlein, L. Helden, A. Gambassi, S. Dietrich and C. Bechinger, *Nature*, 2008, **451**, 172–175.
3  S. Buzzaccaro, J. Colombo, A. Parola and R. Piazza, *Phys. Rev. Lett.*, 2010, **105**, 198301.
4  N. Gnan, E. Zaccarelli and F. Sciortino, *Nat. Commun.*, 2014, **5**, 3267.
5  J. R. Edison, N. Tasios, S. Belli, R. Evans, R. van Roij and M. Dijkstra, *Phys. Rev. Lett.*, 2015, **114**, 038301.
6  S. Stuij, M. Labbe-Laurent, T. Kodger, A. Maciolek and P. Schall, *Soft Matter*, 2017, DOI: 10.1039/C7SM00599G.
7  D. Bonn, J. Otwinowski, S. Sacanna, H. Guo, G. Wegdam and P. Schall, *Phys. Rev. Lett.*, 2009, **103**, 156101.
8  M. T. Dang, A. V. Verde, P. G. Bolhuis and P. Schall, *J. Chem. Phys.*, 2013, **139**, 094903.
9  V. D. Nguyen, S. Faber, Z. Hu, G. H. Wegdam and P. Schall, *Nat. Commun.*, 2013, **4**, 1584.
10  D. J. Kraft, R. Ni, F. Smallenburg, M. Hermes, K. Yoon, D. A. Weitz, A. van Blaaderen, J. Groenewold, M. Dijkstra and W. K. Kegel, *Proc. Natl. Acad. Sci. U. S. A.*, 2012, **109**, 10787–10792.
11  Q. Chen, S. C. Bae and S. Granick, *Nature*, 2011, **469**, 381–384.
12  Y. Wang, Y. Wang, D. R. Breed, V. N. Manoharan, L. Feng, A. D. Hollingsworth, M. Weck and D. J. Pine, *Nature*, 2012, **491**, 51–55.
13  D. J. Kraft, J. Groenewold and W. K. Kegel, *Soft Matter*, 2009, **5**, 3823–3826.
14  A. Nguyen, A. C. Newton, S. J. Veen, D. Kraft, P. G. Bolhuis and P. Schall, *Adv. Mater.*, 2017, DOI: 10.1002/adma.201700819.
15  B. V. Derjaguin and L. Landau, *Acta physicochim. URSS*, 1941, **14**, 633–662.
16  E. Verwey and J. T. G. Overbeek, *Theory of Stability of Lyophobic Solids*, 1948.
17  S. Asakura and F. Oosawa, *J. Chem. Phys.*, 1954, **22**, 1255–1256.
18  N. Kern and D. Frenkel, *J. Chem. Phys.*, 2003, **118**, 9882–9889.
19  D. Chandler and H. C. Andersen, *J. Chem. Phys.*, 1972, **57**, 1930.
20  L. J. Lowden and D. Chandler, *J. Chem. Phys.*, 1974, **61**, 5228–5241.
21  B. M. Ladanyi and D. Chandler, *J. Chem. Phys.*, 1975, **62**, 4308–4324.
22  J. D. Cox, *J. Chem. Soc.*, 1952, 4606.
23  J. N. Israelachvili, *Intermolecular and surface forces: revised third edition*, Academic Press, 2011.
24  R. L. Henderson, *Phys. Lett. A*, 1974, **49**, 197–198.
25  G. Munaò, F. Gámez, D. Costa, C. Caccamo, F. Sciortino and A. Giacometti, *J. Chem. Phys.*, 2015, **142**, 224904.
26  J. Talbot and D. J. Tildesley, *J. Chem. Phys.*, 1985, **83**, 6419–6424.
27  J.-P. Hansen and I. R. McDonald, *Theory of Simple Liquids*, Academic Press, San Diego, 2013.
28  D. Frenkel and B. Smit, *Understanding molecular simulation: from algorithms to applications*, Academic Press, 2001, vol. 1.
29  A. Bhattacharyay and A. Troisi, *Chem. Phys. Lett.*, 2008, **458**, 210–213.
30  U. Nellen, J. Dietrich, L. Helden, S. Chodankar, K. Nygård, J. F. van der Veen and C. Bechinger, *Soft Matter*, 2011, **7**, 5360–5364.
31  M. G. Noro and D. Frenkel, *J. Chem. Phys.*, 2000, **113**, 2941–2944.
32  G. A. Vliegenthart and H. N. W. Lekkerkerker, *J. Chem. Phys.*, 2000, **112**, 5364–5369.

33  B. Freasier, D. Jolly and R. Bearman, *Mol. Phys.*, 1976, **31**, 255–263.

34  B. Barboy and W. Gelbart, *J. Chem. Phys.*, 1979, **71**, 3053–3062.

35  F. Romano, C. De Michele, D. Marenduzzo and E. Sanz, *J. Chem. Phys.*, 2011, **135**, 124106.

36  M. Holmes-Cerfon, *Annu. Rev. Condens. Matter Phys.*, 2017, **8**, 77–98.

37  G. van Anders, D. Klotsa, N. K. Ahmed, M. Engel and S. C. Glotzer, *Proc. Natl. Acad. Sci. U. S. A.*, 2014, **111**, E4812–E4821.

38  G. Avvisati, T. Vissers and M. Dijkstra, *J. Chem. Phys.*, 2015, **142**, 084905.